

# Quick AS NEXAFS Tool (QANT): a program for NEXAFS loading and analysis developed at the Australian Synchrotron

Eliot Gann,<sup>a,b</sup> Christopher R. McNeill,<sup>a</sup> Anton Tadich,<sup>b</sup> Bruce C. C. Cowie<sup>b</sup> and Lars Thomsen<sup>b\*</sup>

Received 7 July 2015

Accepted 5 October 2015

Edited by R. W. Strange, University of Liverpool, UK

**Keywords:** NEXAFS; absorption spectroscopy; instant analysis; peak fitting; compositional analysis; normalization; computer programs; *Quick AS NEXAFS Tool (QANT)*.

**Supporting information:** this article has supporting information at journals.iucr.org/s

<sup>a</sup>Department of Materials Science and Engineering, Monash University, Wellington Road, Clayton, Victoria 3800, Australia, and <sup>b</sup>Australian Synchrotron, 800 Blackburn Road, Clayton, Victoria 3168, Australia.

\*Correspondence e-mail: soft-xray@synchrotron.org.au

An analysis program for near-edge X-ray absorption fine-structure (NEXAFS) spectra has been developed and implemented at the soft X-ray beamline of the Australian Synchrotron. The program allows for instant viewing of corrected data channels including normalizations to a standard, double normalizations when the standard itself has an undesired spectral response, and background subtraction. The program performs simple compositional analysis and peak fitting and includes rapid common calculations such as the average tilt angle of molecules with respect to the surface, and the determination of the complex index of refraction, which previously required intensive manual analysis. These functionalities make common manipulations carried out with NEXAFS data quick and straightforward as spectra are collected, greatly increasing the efficiency and overall throughput of NEXAFS experiments.

## 1. Introduction

Near-edge X-ray absorption fine-structure (NEXAFS) spectroscopy is a powerful technique which has the ability to reveal the molecular structure and orientation at surfaces, interfaces and within thin films (Williams *et al.*, 1980; Johnson *et al.*, 1983; Rosenberg *et al.*, 1986; Stöhr *et al.*, 1987; Outka & Stöhr, 1988; Ade, 1994, 1997, 2004; Watts *et al.*, 2006; Gann *et al.*, 2014; Luzio *et al.*, 2014; Szumilo *et al.*, 2014). Depending upon the energy of an absorbed X-ray, a core-level electron can be excited to an unoccupied but bound molecular orbital, or to a free state above the vacuum level. The critical aspect is that the absorption cross section of X-rays near the binding energy of a core electron is highly sensitive to the local bonding environment of the atom; by carefully recording the absorption spectrum in this near-edge region, this bonding environment can be probed.

Although a direct absorption measurement is challenging, there are several methods of *indirectly* measuring an absorption spectrum, including the total electron yield (TEY), partial electron yield (PEY), Auger electron yield (AEY), fluorescence yield (FY) and attenuation of the incident X-ray flux (X-ray transmission). Each of these modes measures slightly different aspects of the absorption process; for instance, the depth sensitivity of each probe can vary considerably. For this reason several of these detection modes are collected simultaneously at the Soft X-ray (SXR) beamline of the Australian Synchrotron (AS). Each of the measurement channels requires different levels of correction, normalization and scaling to solve for an effective absorption. Spectra are then

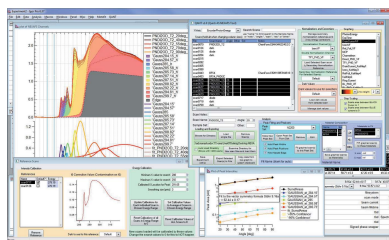




**Figure 1**  
*QANT* window, with a set of typical data being analysed. Each element will be covered in the proceeding figures, each of which was created within *QANT*.

analysed in one of several common ways: peak fitting, compositional analysis, average tilt angle determination and/or calculation of the refractive index.

To aid in these common tasks, from data loading through analysis, we present a new analysis program called *Quick AS NEXAFS Tool (QANT)*; an image of the interface is shown in Fig. 1. Developed in the *IgorPro* mathematical programming environment (WaveMetrics Inc., Lake Oswego, Oregon, USA), *QANT* loads NEXAFS data files as they are written at the SXR beamline of the AS and enables both automatic correction of X-ray energy and normalization of intensity (see video 1 of the supporting information). Though *QANT* has been developed to automate data normalization and simplify data analysis on the AS SXR beamline, the program has an expanding functionality to load spectra collected from other facilities as well as output from theoretical calculations. Following the loading and normalization of data, *QANT* streamlines common NEXAFS analysis tasks, providing a platform for further analysis and exporting of corrected and reduced data.

## 2. Data correction, normalization and scaling

As discussed elsewhere (Watts *et al.*, 2006), a raw NEXAFS scan requires several corrections in order to convert the measured values into a true absorption spectrum. We can split these corrections into four types: measurement and spectral offsets, normalization to incident flux, incident flux spectral contaminant corrections (secondary normalization), and scaling data for comparisons between spectra. These can consist of purely mathematical transformations, point-by-point corrections or scan-to-scan corrections. Point-by-point corrections adjust for random changes to the X-ray beam properties during each individual measurement (such as X-ray flux), for which each individual data point within a scan will

require a slightly different correction than all of the other data points. Scan-to-scan corrections include those corrections which are static or change slowly enough that for all the measurements within a single scan only a single value or occasionally measured reference spectrum is needed (such as energy correction). Mathematical transformations like the conversion of a transmission measurement to absorption for a photodiode placed behind the sample. This mathematical transformation is carried out by taking the negative logarithm of the transmitted signal. Periodic calibration scans, including dark value scans and secondary normalization reference scans are collected during experiments whereas additional reference channels are recorded simultaneously with each measurement, so that a single NEXAFS

scan consists of several channels of data in addition to several channels used for corrections.

### 2.1. Measurement offsets

Each measurement has additive and multiplicative offsets which can be corrected scan to scan. The basic additive offset for each signal is the dark level: a nonzero measured value when no X-rays are present in the system. This can be measured by a single data set collected under the same experimental conditions but with a far-upstream shutter blocking X-rays from entering the beamline. Thus any contribution from ambient lighting or electronic backgrounds which are not related to the X-rays interacting with the sample can be quantified and subtracted from the raw data for each measurement channel.

### 2.2. X-ray energy offsets

Correction of the X-ray energy at the SXR beamline can involve a point-by-point encoder measurement which can catch occasional differences between the desired wavelength and the calculated wavelength based on the angles and positions of the X-ray optics, monochromator and slits. Unfortunately, the encoded values of wavelength, although quite accurate within a given scan, may be offset and drift slightly from scan to scan (Cowie *et al.*, 2010). For this reason, an additional energy calibration spectrum is measured simultaneously with the sample spectra using a small portion of the beam. Based on the range of energies in the scan, different calibration standards, with known peaks or edges that span the X-ray energy range of the beamline ( $\sim 100$  eV to  $\sim 3000$  eV), are chosen. After correcting for point-by-point variations within a scan, an offset from a known peak location measured in the calibration spectrum can set the absolute energy scale for the whole scan. An example of X-ray energy correction is

shown in Fig. 2. The normalized and scaled TEY signal from a common organic semiconducting polymer and the reference spectra, in this case highly oriented pyrolytic graphite (HOPG), taken simultaneously with each scan is shown in Figs. 2(a) and 2(b), respectively, representing the spectra of the same material taken at different times during an experiment run. Correcting the energy scale of each scan by locating and shifting the peak in the reference spectra to its known energy position (Fig. 2d), the two data channels are revealed to be identical (Fig. 2c), indicating spectral drift between measurements and hence incorrect normalization. The spectral changes between Figs. 2(a) and 2(c) are due to the additional X-ray energy offset between the spectra and the secondary normalization reference spectra, which results in incorrect normalization when the energy scales are not aligned. In order to perform correct normalization, it is important to adjust the X-ray energy scales for each data set as well as for the separate secondary normalization reference spectra (discussed in the next section) prior to subsequent corrections.

### 2.3. Flux normalizations

The flux of X-rays varies at different X-ray energies at the SXR beamline because of the source efficiency and the reflectivity of the optical components. This is particularly the case across the absorption edges of the materials and common contaminants on the mirrors, including oxygen and carbon. There is a particularly sharp contamination feature around 284 eV (near the carbon 1s binding energy) referred to as the ‘carbon dip’, which dramatically changes the reflectivity of mirrors at the carbon edge and hence the flux of X-rays through the beamline (Koide *et al.*, 1986; Kurt *et al.*, 2002; Gann *et al.*, 2012). In addition, the dynamics of the flux from one measurement to the next can vary due to a variety of reasons from the source (in this case a soft X-ray undulator), through to the end of the beamline, so simply having a single measurement of the typical spectral flux of the beamline is not sufficient. For this reason, a partially transmissive (approximately 50%) Au mesh is placed before the sample in order to monitor and normalize the NEXAFS signal to the real X-ray flux profile during each measurement. For point-by-point corrections, the Au mesh records any ephemeral changes to the beam flux. The Au mesh is chosen because it can measure a representative part of the beam and does not act as an energy filter because essentially all the photons which hit the mesh are absorbed, producing a drain current. This drain current, for the typically short energy ranges used in NEXAFS, is essentially proportional to the incident flux. The remaining photons pass unaffected through the gaps in the mesh and are incident on the sample.

It is nontrivial to measure the precise portion of the beam which is removed by the Au mesh (as this varies with the beam footprint and precise mesh orientation) and hence the relationship of the Au mesh drain current to the actual number of photons per second incident onto the sample, due to energy-dependent effects from contaminants on the Au mesh. Often

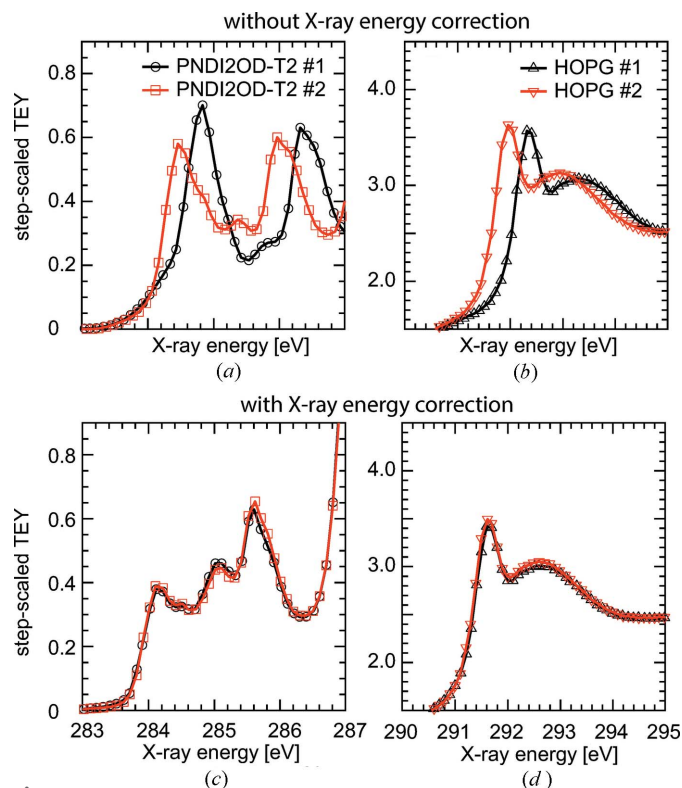


**Figure 2** Example of spectral energy correction applied to NEXAFS data collected several hours apart at the AS. (a) Spectra from poly[[N,N'-bis(2-octyldodecyl)-1,4,5,8-naphthalenedicarboximide-2,6-diyl]-alt-5,5'-(2,2'-bithiophene)] [P(NDI2OD-T2)] after normalizations. (b) Uncorrected reference spectra of HOPG taken concurrently with the spectra in (a). (c) The same spectra of P(NDI2OD-T2) with the energy scale of each corrected by the location of the exciton peak at 291.65 eV (Watts & Ade, 2008) in HOPG after which normalizations are performed. (d) The corrected HOPG reference spectra with the characteristic exciton absorption peak corrected to 291.65 eV.

the adventitious contaminants of the mesh which alter the drain current are the same elements that are present on the X-ray optics, the effect of which we are trying to normalize away. For instance, the carbon contamination on the Au mesh itself actually increases the drain current from the mesh above the carbon edge (see Fig. 3a), resulting in an apparently increased mesh drain current in the carbon dip, where fewer photons are actually travelling down the beamline.

The most accurate measurement of actual photon flux is a calibrated photodiode (Fig. 3a) (Husk *et al.*, 1991). For a photodiode, the spectral response is well understood and surface contaminations do not affect the photodiode signal, which is produced within the bulk of the diode. A separate scan with the photodiode in place of the sample allows calibration of the response of the Au mesh as a function of the X-ray wavelength (Fig. 3b). When we measure the spectral response of the normalization channel in this way, we can then use this measurement as a secondary normalization reference for the Au mesh signal taken simultaneously with each sample. It is important to note that in order to make this secondary normalization successfully, X-ray energy calibration of both scans is required beforehand; note the difference in spectral



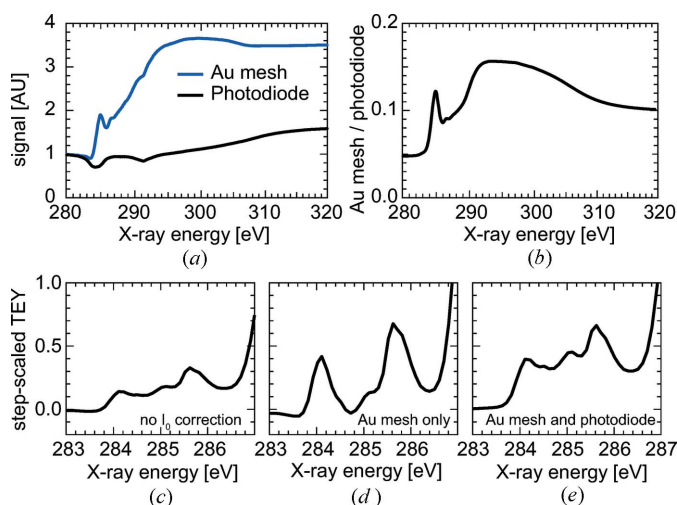


**Figure 3**

(a) Raw signal from a contaminated Au mesh and a photodiode in the place of the sample. The Au mesh shows extra signal due to contamination. (b) Corrected Au mesh signal [ratio of the raw signals from (a)]; contaminated Au mesh signal/photodiode signal]. TEY spectra from P(NDI2OD-T2) with (c) no spectral correction, (d) correction of signal by Au mesh alone, and (e) correction by corrected Au mesh signal shown in (b). All spectra have been previously X-ray energy corrected.

shape between Figs. 2(a) and 2(c). The difference in correcting by just the Au mesh signal (Fig. 3d) and the corrected Au mesh signal (Fig. 3e) is critical for the accurate representation of spectral features.

#### 2.4. Measurement scaling

Further scan-to-scan corrections can include corrections for instrument technique sensitivity, including those that vary with the incident angle between the X-rays and the surface. For instance, when comparing the TEY signal measured at different incident angles (Fig. 4a), the TEY signal will increase at grazing-incident angles, where the X-rays have a longer interaction path within the first few nanometres of the surface. Increased X-ray absorption within the first few nanometres means that more electrons are produced in this region, where they can escape the surface and contribute to the TEY signal. To calculate precise absorption coefficients, it would be necessary to correct for the percentage of absorption events which produce electrons that escape the surface. However, when doing several scans at different angles, the absolute level of absorption is often not needed and an empirical scaling to the step edge can be made. Because the X-rays interact with the same chemical structure, just at

different angles, the angle-independent bare atom atomic step edge far from the near-edge region remains constant. This allows each spectrum to be scaled below and far above the edge to 0 and 1, respectively (Watts *et al.*, 2006, 2011), so that angular-dependent spectral differences can be examined relative to each other (Fig. 4b). Because this is typically the quickest method of scaling, ionization step scaling is the method used throughout this work. Alternatively, the spectra can be spliced onto theoretical bare atom absorption spectra (Henke *et al.*, 1993; Watts, 2014) for more quantitative analysis, such as calculation of optical constants and refractive indices [Figs. 4(c) and 4(d)] described in §3.3.

### 3. Data analysis

Once the NEXAFS spectra are corrected, normalized and scaled, there are a number of widely used analysis methods that can be performed on the data. The most common are peak fitting, tilt angle calculations, materials compositional analysis and calculation of the refractive index.

#### 3.1. Peak fitting

NEXAFS spectra from complex materials will often consist of many resonances, each of which corresponds to a different

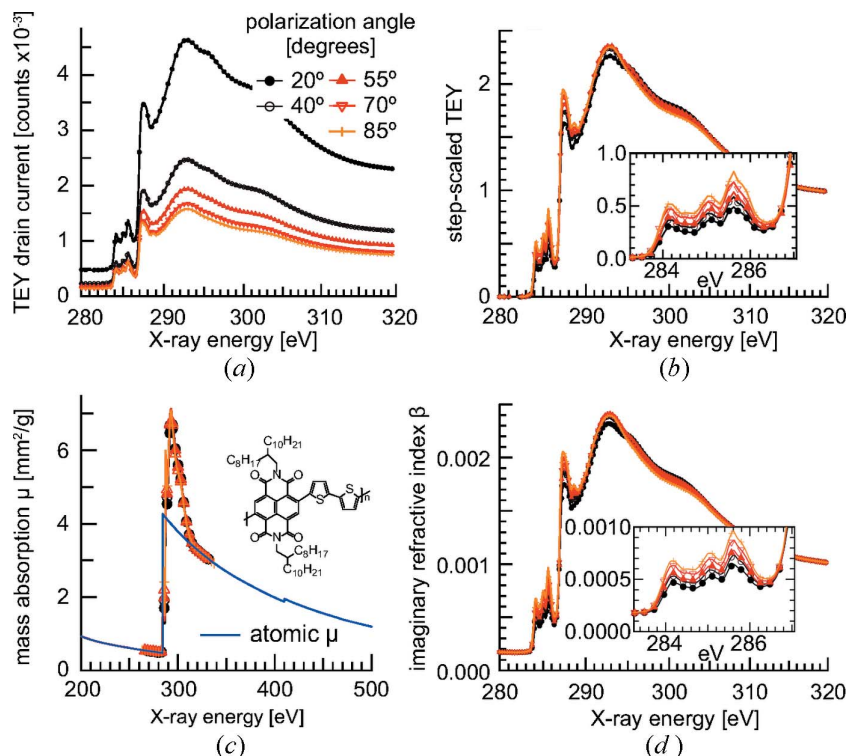


**Figure 4**

(a) Corrected TEY signal from P(NDI2OD-T2) at different incident angles, showing the artificially increased intensity of shallower angles. (b) The same set of data step-scaled to 0 at the pre-edge (280 eV) and 1 at the post-edge (320 eV). Inset is a closer view of the  $\pi^*$  resonances from around 284–286 eV. (c) The bare-atom spectra (Henke *et al.*, 1993) calculated from the molecular structure (inset) with overlaid measured NEXAFS spectra, which have been scaled to match the bare-atom mass absorption spectra at the edges of the data range. (d) The same spectra from (a), scaled to the bare atom mass absorption, and corrected to the imaginary part of the index of refraction using a nominal density of  $1 \text{ g cm}^{-3}$ . Inset is a closer look at the  $\pi^*$  resonances from around 284–286 eV.

transition from the occupied core state to an unfilled final state. These resonances can generally be modelled as common peak shapes (Lorentzian and Gaussian) (Watts *et al.*, 2006; Stöhr, 1992) with a background of the bare atomic ionization potential. Thus the first step in many analyses is to decompose the NEXAFS spectra into a set of peaks, which can then be assigned to different available and physically reasonable transitions. At the carbon 1s absorption edge, for instance, excitations below 286 eV can generally be attributed to the carbon 1s → C=C π\* transition, as often used as an example in this work. Other common transitions have been identified elsewhere (Hähner *et al.*, 1991).

Peak fitting in *QANT* is made through the interactive creation of peak sets (see video 2 of the supporting information). These sets of peaks can be imported from spreadsheets or text files, or created either by using semi-automated peak finding methods in *IgorPro* or manually. Peak types include Gaussian, Lorentzian, asymmetric Gaussian and Voigt profiles, whereas backgrounds include empirical ionization potential step edges, as well as constant, linear, cubic and log cubic functions. Peaks can be drawn onto the spectra and refined in an iterative manner to build up a physically relevant set of peaks which adequately fit the spectra. Having created this peak set, it can then be used to simultaneously fit many data sets, with the option of allowing peaks to be fixed in position or width among the multiple data sets and letting the background function be fixed or vary between each spectrum. The resulting multiple spectra fit can be displayed and plotted in a variety of ways. For instance, the tilt angle of each individual resonance (peak) or any combination of resonances can be plotted and fit if multiple scans are selected each having a defined polarization angle (the angle between the polarization vector and the surface, which is automatically read from the metadata in each scan). Fig. 5 shows the default output generated when fitting a set of five scans with different polarization angles. The component peaks are shown (as in Fig. 5a) and, when one or more peaks are chosen in the resulting peak fit window, a graph is generated (Fig. 5b) from which the tilt angle can be determined. If we choose the main peaks making up the π\* resonances, we can see the resulting average tilt angle of those resonances from equation 9.16a in *NEXAFS Spectroscopy* (Stöhr, 1992), along with the uncertainties. For peaks with different symmetry, we can also choose the appropriate tilt angle equation to use in each case.

### 3.2. Materials composition

Another common application of NEXAFS is to use the spectra of known materials as a quantitative fingerprint to find the composition of a mixed system (see video 3 of the supporting information). Thus, in a mixture of materials, if the spectra of the individual constituents is known (or measured) the percentage of each material in the mixture can be solved, as long as there is minimal chemical reaction occurring between the components, which would change the spectra. Materials composition analysis is common in spectral mapping of spot to spot inhomogeneities and for determination of

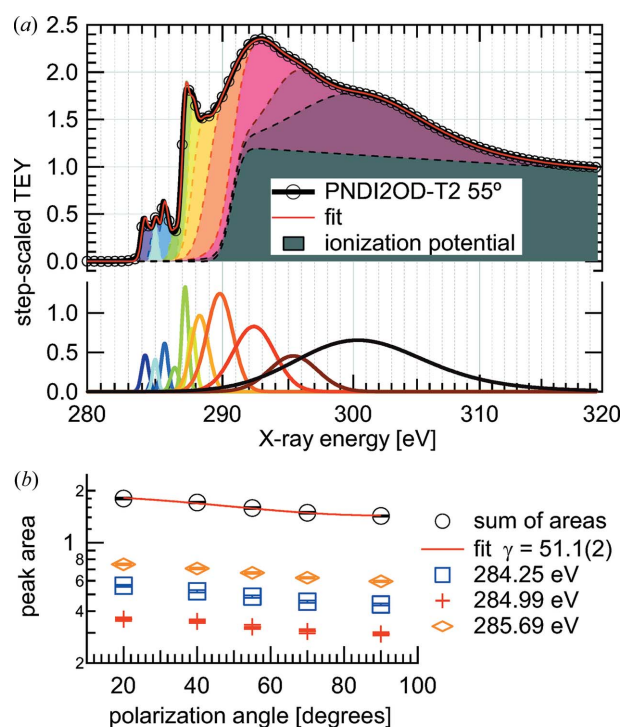


**Figure 5**  
 (a) An example peak fit produced by *QANT* of P(NDI2OD-T2) at a 55° incident angle, showing the component peaks below and the contribution to the spectra above. All peak shapes are Gaussian except the peak at ~300 eV, which is an exponential modified Gaussian. The background peak is an empirical ionization step potential. (b) A tilt angle graph produced by *QANT* when several scans at different angles are chosen to fit simultaneously. In the resulting fit, three peaks which constitute the π\* manifold are chosen, and the sum of the areas is fit to the vector symmetry equation 9.16a given by Stöhr (1992).

capping layer composition (Deshmukh *et al.*, 2015). In *QANT*, the quantitative fingerprinting of materials is implemented as shown in Fig. 6(a). For each data set selected, a graph such as that in Fig. 6(a) is produced, showing the components, the original data set and the best linear composition fit of the components. The number of constituents is unlimited. If many data sets are selected, a table of the results is produced.

### 3.3. Calculating the refractive index

Finally, to quantitatively analyse resonant X-ray scattering patterns or resonant X-ray reflectivity profiles, knowing the optical constants – that is, the complex refractive index – of materials in the system is critical. Absorption is the imaginary portion of the refractive index and the Kramers–Kronig relations allow for determination of the real part of the refractive index if a wide enough range of absorption is measured, as described in detail elsewhere (Yan *et al.*, 2013; Watts, 2014). It is important to note that the required parameters, in addition to the near-edge spectra, are the density and the chemical formula. Sample homogeneity is of importance in order to ensure that the chemical formula is representative of the signal measured. The chemical formula allows one to build up an atomic spectrum from the linear combination of each individual atom (Henke *et al.*, 1993), whilst the density scales the spectrum. If the NEXAFS spectrum that is

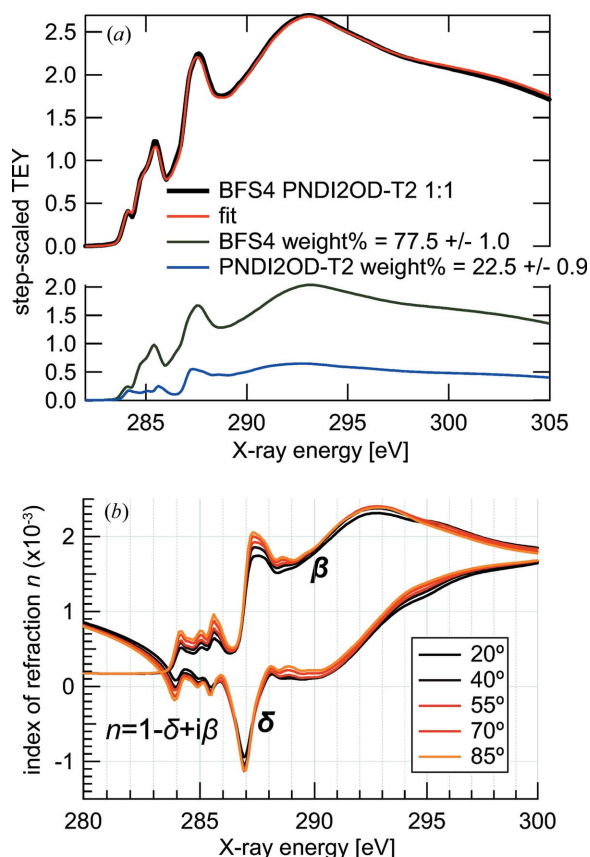


**Figure 6**

(a) The materials composition fit produced by *QANT* for a mixture of P(NDI2OD-T2) and BFS4 (Deshmukh *et al.*, 2015). The result shows an enrichment of BFS4 at the surface. (b) The full calculated index of refraction for P(NDI2OD-T2). The imaginary component of the refractive index,  $\beta$ , as previously shown in Fig. 4(d), is the absorptive part of the refractive index, whereas the real deviation from 1,  $\delta$ , is calculated from  $\beta$  by the Kramers–Kronig relations as described in the text if a chemical formula and density are input into *QANT*.

measured is spliced into the bare-atom spectrum, the Kramers–Kronig calculation can determine the effective real part of the index of refraction, as shown in Fig. 6(b). Thus, if a chemical formula and a density for a given spectra are known and entered into *QANT*, the program can automatically calculate the full complex index of refraction. In addition, if two spectra are selected, the contrast (Gann *et al.*, 2012), which is both the wavelength-dependent total scattering intensity expected in a mixture of the two materials and the proportional reflectivity at interfaces between the two materials, is calculated and displayed.

#### 4. Methods

Using the *IgorPro* environment allows the calculations to be made at each step as well as to be easily accessible and explored by the user. Each measurement channel is stored as an array (called a wave in *IgorPro* language) in a separate data folder. Thus for each step of each calculation, the entire data structure is copied into a different data folder. This allows the corrected data set at each step of correction to be calculated only once as needed, and updated and accessed efficiently. For

example, if a data set has been processed through steps A–E which are ordered operations (say these are, respectively, dark-level correction, X-ray energy correction, normalization, secondary normalization, and step-edge scaling), the results of each of these operations is stored in a separate data folder. If the calculation at level D is changed (that is, a new photodiode mesh scan is chosen), then data folders containing step D and later (step E in this case) are deleted, and recalculated with the new parameters, leaving the data at step C unaltered. For any future calculations or display of data, the highest level folder which contains that data will be used. Upon displaying or exporting data, the full history of alterations to each data set is available in metadata.

In addition to the measurement channels in each scan, there are a number of parameters included in the scan file as metadata which are read and used for analysis. In particular, this includes the comments from the user upon starting the scan (including the sample name, chemical formula and density if it is entered), and all of the motor positions and beam parameters which are static during the scan but which may change between scans. All of these parameters can be viewed or graphed as desired by the user (*e.g.* to plot a slit position *versus* measurement time) to monitor changes during an experiment. In addition, sample positioning motors are often needed in analysis, for instance in tilt angle calculations, so *QANT* automatically reads these parameters into the proper fields for later analysis.

Peak fitting is performed using a least-squares Levenberg–Marquardt algorithm using an interactive multiple peak fit, with user-defined constraints. During the initial peak set creation, user intervention is often required to force physical representation of transitions, *i.e.* to ensure multiple narrow excitations are not approximated by a single wide peak.

Tilt angle fitting is made by fitting the peak area or sum of peak areas as chosen by the user *versus* polarization angle to various formulas depending on the molecular symmetry. If the symmetry of the molecular orbital in question is planar, equation 9.17a given by Stöhr (1992) can be used if the molecular orbital instead has a vector symmetry (typical for  $1s$  to  $\pi^*$  transitions in organic electronics, in which the  $\pi^*$  orbitals are aligned normal to the planar face of the molecule), equation 9.16a (Stöhr, 1992) can be used. If there is in-plane alignment, the corresponding equations 9.15a and 9.14a (Stöhr, 1992) can also be chosen. Uncertainty in peak intensity is propagated through to uncertainty in the final tilt angle determination and one sigma confidence bands are plotted along with the fit. This allows for effortless determination of the quality of the fit and enables easy identification of outlying scans which can be collected again in a timely manner.

Compositional fitting is accomplished by a least-squares linear decomposition. Depending upon the normalization of the reference spectra and the fit spectra, the resulting fit may be relative to the atomic density of the components (if scaled to pre- and post-edge) or molecular weight percentage of components (with input of the chemical formula) or volume percentage (with the additional input of the density of the constituents).



## 5. Conclusion

We have presented a novel program designed for NEXAFS analysis at the SXR beamline of the Australian Synchrotron, named *QANT*. This program allows a live look at reduced data with instant offset corrections, normalizations, scaling and calculations which are often made with NEXAFS data. Though recently commissioned, *QANT* is now being used on a regular basis and it has already proven useful for a number of research groups (Stacey *et al.*, 2015; Gann *et al.*, 2014; Deshmukh *et al.*, 2015; Huang *et al.*, 2014; Luzio *et al.*, 2014; Szumilo *et al.*, 2014). This instant analysis enables timely identification of possible measurement problems and particularly subtle issues such as beam damage and hence provides an overall more efficient use of a beam time session with added confidence in the scientific outcomes. The ease of applying common analysis methods consistently and quickly enables efficient offline analysis as well, decreasing overall times between experimental acquisition and publication. Further developments of *QANT* include determining extreme polarized spectra from angular-dependent spectra (Schuettfort *et al.*, 2012) and data formats from different NEXAFS facilities as well as theoretical calculations. Although designed for the AS SXR NEXAFS data system, spectra from other NEXAFS facilities [at the Advanced Light Source (Gann *et al.*, 2012) and NanoXAS beamline of the SLS (Watts *et al.*, 2015)] have been successfully loaded into *QANT* for further analysis and work is underway to write a general NEXAFS file loading module. A benefit of the *IgorPro* platform and the modular nature of *QANT* is that loading the data into waves in a data folder is all that is generally required. The identification of which data channel corresponds to what normalization is chosen by the user. Benefits of collecting spectra at the SXR beamline are the simultaneous signal and normalization channels as well as extensive metadata contained in each scan, which make instant analysis possible. Although sequential measurements and less extensive metadata at other facilities can require manual intervention and slow down data loading and correction process, the benefits of the ease and efficiency of analysis in *QANT* remain.

## Acknowledgements

This research was designed and commissioned at the Australian Synchrotron at the SXR beamline (Cowie *et al.*, 2010).

## References

Ade, H. (1994). *Synchrotron Radiat. News*, **7**, 11.  
 Ade, H. (1997). *X-ray Microscopy and Spectromicroscopy*, edited by J. Thieme, G. Schmahl, E. Umbach and D. Rudolph. Berlin: Springer-Verlag.

Ade, H. (2004). *Encyclopedia of Polymer Science and Technology*, 3rd ed., edited by J. Kroschwitz. New York: Wiley.  
 Cowie, B. C. C., Tadich, A. & Thomsen, L. (2010). *AIP Conf. Proc.* **1234**, 307–310.  
 Deshmukh, K. D., Qin, T., Gallaher, J. K., Liu, A. C. Y., Gann, E., O'Donnell, K., Thomsen, L., Hodgkiss, J. M., Watkins, S. E. & McNeill, C. R. (2015). *Energy Environ. Sci.* **8**, 332–342.  
 Gann, E., McNeill, C. R., Szumilo, M., Sirringhaus, H., Sommer, M., Maniam, S., Langford, S. J. & Thomsen, L. (2014). *J. Chem. Phys.* **140**, 164710.  
 Gann, E., Young, A. T., Collins, B. A., Yan, H., Nasiatka, J., Padmore, H. A., Ade, H., Hexemer, A. & Wang, C. (2012). *Rev. Sci. Instrum.* **83**, 045110.  
 Hähner, G., Kinzler, M., Wöll, C., Grunze, M., Scheller, M. K. & Cederbaum, L. S. (1991). *Phys. Rev. Lett.* **67**, 851–854.  
 Henke, B. L., Gullikson, E. M. & Davis, J. C. (1993). *At. Data Nucl. Data Tables*, **54**, 181–342.  
 Huang, W., Gann, E., Thomsen, L., Dong, C., Cheng, Y.-B. & McNeill, C. R. (2014). *Adv. Energy Mater.* **5**, 1401259.  
 Husk, D. E., Tarrio, C., Benitez, E. L. & Schnatterly, S. E. (1991). *J. Appl. Phys.* **70**, 3338–3344.  
 Johnson, A. L., Muetterties, E. L. & Stöhr, J. (1983). *J. Am. Chem. Soc.* **105**, 7183–7185.  
 Koide, T., Sato, S., Shidara, T., Niwano, M., Yanagihara, M., Yamada, A., Fujimori, A., Mikuni, A., Kato, H. & Miyahara, T. (1986). *Nucl. Instrum. Methods Phys. Res. A*, **246**, 215–218.  
 Kurt, R., van Beek, M., Crombeen, C., Zalm, P. & Tamminga, Y. (2002). *Proc. SPIE*, **4688**, 702–709.  
 Luzio, A., Fazzi, D., Nübling, F., Matsidik, R., Straub, A., Komber, H., Giussani, E., Watkins, S. E., Barbatti, M., Thiel, W., Gann, E., Thomsen, L., McNeill, C. R., Caironi, M. & Sommer, M. (2014). *Chem. Mater.* **26**, 6233–6240.  
 Outka, D. A. & Stöhr, J. (1988). *Springer Series in Surface Science*, Vol. 10, *Chemistry and Physics of Solid Surfaces VII*, edited by R. Vanselow and R. F. Howe, p. 201. Berlin: Springer-Verlag.  
 Rosenberg, R. A., Love, P. J. & Rehn, V. (1986). *Phys. Rev. B*, **33**, 4034–4037.  
 Schuettfort, T., Watts, B., Thomsen, L., Lee, M., Sirringhaus, H. & McNeill, C. R. (2012). *ACS Nano*, **6**, 1849–1864.  
 Stacey, A., O'Donnell, K. M., Chou, J.-P., Schenk, A., Tadich, A., Dentschuk, N., Cervenka, J., Pakes, C., Gali, A., Hoffman, A. & Praver, S. (2015). *Adv. Mater. Interfaces*, **2**, doi:10.1002/admi.201500079.  
 Stöhr, J. (1992). *NEXAFS Spectroscopy*. New York: Springer-Verlag.  
 Stöhr, J., Outka, D. A., Baberschke, K., Arvanitis, D. & Horsley, J. A. (1987). *Phys. Rev. B*, **36**, 2976–2979.  
 Szumilo, M. M., Gann, E. H., McNeill, C. R., Lemaure, V., Oliver, Y., Thomsen, L., Vaynzof, Y., Sommer, M. & Sirringhaus, H. (2014). *Chem. Mater.* **26**, 6796–6804.  
 Watts, B. (2014). *Opt. Express*, **22**, 23628–23639.  
 Watts, B. & Ade, H. (2008). *J. Electron Spectrosc. Relat. Phenom.* **162**, 49–55.  
 Watts, B., Swaraj, S., Nordlund, D., Lüning, J. & Ade, H. (2011). *J. Chem. Phys.* **134**, 024702.  
 Watts, B., Thomsen, L. & Dastoor, P. C. (2006). *J. Electron Spectrosc. Relat. Phenom.* **151**, 105–120.  
 Watts, B., Warnicke, P., Pilet, N. & Raabe, J. (2015). *Phys. Status Solidi A*, **212**, 518–522.  
 Williams, R. S., Denley, D., Shirley, D. A. & Stoehr, J. (1980). *J. Am. Chem. Soc.* **102**, 5717–5723.  
 Yan, H., Wang, C., McCarn, A. R. & Ade, H. (2013). *Phys. Rev. Lett.* **110**, 177401.